Grain rotation mechanisms in nanocrystalline materials: Multiscale observations in Pt thin films

Yuan Tian[1], Xiaoguo Gong[2], Mingjie Xu[3], Caihao Qiu[4], Ying Han[1], Yutong Bi[1], Leonardo Velasco Estrada[5,6], Evgeniy Boltynjuk[5], Horst Hahn[5,7], Jian Han[4]*, David J. Srolovitz[2,8]*, Xiaoqing Pan[1,3,9]*

Near-rigid-body grain rotation is commonly observed during grain growth, recrystallization, and plastic deformation in nanocrystalline materials. Despite decades of research, the dominant mechanisms underlying grain rotation remain enigmatic. We present direct evidence that grain rotation occurs through the motion of disconnections (line defects with step and dislocation character) along grain boundaries in platinum thin films. State-of-the-art in situ four-dimensional scanning transmission electron microscopy (4D-STEM) observations reveal the statistical correlation between grain rotation and grain growth or shrinkage. This correlation arises from shear-coupled grain boundary migration, which occurs through the motion of disconnections, as demonstrated by in situ high-angle annular dark-field STEM observations and the atomistic simulation–aided analysis. These findings provide quantitative insights into the structural dynamics of nanocrystalline materials.

A polycrystalline material is an aggregate of crystallites with different lattice orientations. The crystallites (i.e., grains) undergo near-rigid-body rotation during microstructure evolution. Such grain rotation has been widely observed in polycrystalline materials, especially in nanocrystalline materials, during recrystallization (*1*, *2*), plastic deformation (*3*, *4*), and grain growth (*5*–*9*). Grain rotation greatly affects microstructure evolution [e.g., modifying the grain growth kinetics (*1*, *2*, *5*, *7*, *10*–*12*)] and controls texture evolution (*13*, *14*).

Near-rigid-body grain rotation has been described in terms of various grain boundary (GB)–mediated processes, such as GB dislocation climb (*12*, *15*–*17*), GB diffusion (*18*–*21*), GB sliding (*10*, *22*), disclination dipole dynamics (*23*, *24*), and shear-coupled GB migration (*8*, *25*–*28*). While each mechanism may occur under certain restricted circumstances, which GB process most commonly dominates rigid-body grain rotation remains controversial, particularly for grains with high-angle GBs. The rotation of grains delimited by low-angle GBs may be described by GB dislocation climb (*12*, *15*–*17*). This description does not apply to the more common nonspecial, high-angle GBs for which GB dislocations are not well defined. In GB diffusion models, long-range mass transport is rate limiting and hence inapplicable to widely observed fast grain rotation in metals at room temperature (*12*). While GB sliding may occur in bicrystals, sliding is severely restricted by triple junctions (TJs) in polycrystals. Shear-coupled GB migration could be capable of explaining grain rotation involving high-angle GBs. The mechanism of shear-coupled GB migration is the nucleation and propagation of disconnections on the GB (disconnections are GB line defects with both step and dislocation character). However, no experimental evidence exists to support the correlation between disconnection motion and grain rotation (*27*, *29*–*33*), although phenomenological theory has suggested the possibility of rigid-body grain rotation through disconnection motion (*34*). To reveal the dominant mechanism of grain rotation, quantitative correlation between disconnection activity and grain rotation should be built at atomic scale and at statistical level in polycrystalline samples.

Here we present atomic-scale and statistical experimental evidence of disconnection-mediated grain rotation during capillarity-induced grain growth by means of a multiscale in situ scanning transmission electron microscopy (STEM) approach. We conducted atomic-scale imaging to quantitatively correlate each GB migration event with disconnection motion during annealing using in situ high-resolution high-angle annular dark-field STEM (HAADF-STEM). Then, we performed microstructure-scale observations to validate the correlation between grain rotation and grain growth or shrinkage using state-of-the-art in situ four-dimensional STEM (4D-STEM) techniques. We conducted atomistic simulations to assist the interpretation of the experimental observations. Our results not only provide quantitative insights into near-rigid-body grain rotation in polycrystals but also showcase the great potential of multiscale in situ TEM in resolving the debate regarding the representativity of in situ TEM studies on atomic-scale mechanisms.

[1]Department of Materials Science and Engineering, University of California, Irvine, CA, USA. [2]Department of Mechanical Engineering, The University of Hong Kong, Hong Kong, China. [3]Irvine Materials Research Institute (IMRI), University of California, Irvine, CA, USA. [4]Department of Materials Science and Engineering, City University of Hong Kong, Hong Kong, China. [5]Institute of Nanotechnology, Karlsruhe Institute of Technology (KIT), Karlsruhe, Germany. [6]Universidad Nacional de Colombia Sede de La Paz, La Paz, Cesar, Colombia. [7]School of Sustainable Chemical, Biological and Materials Engineering, The University of Oklahoma, Norman, OK, USA. [8]Materials Innovation Institute for Life Sciences and Energy (MILES), The University of Hong Kong, Shenzhen, China. [9]Department of Physics and Astronomy, University of California, Irvine, CA, USA.

***Corresponding author. Email: xiaoqing.pan@uci.edu (X.P.); srol@hku.hk (D.J.S.); jianhan@cityu.edu.hk (J.H.)**

Mesoscale: Grain rotation and GB migration

We conducted our study on ~10-nm-thick platinum (Pt) nanocrystalline thin films produced by magnetron sputtering onto <111>-oriented NaCl substrates. The initial sample exhibits a uniform equiaxed structure with a grain size of ~7 nm and no observable texture [see supplementary text section 1 (*35*) and figs. S1 and S2]. First, we present an atomic-scale observation of the grain rotation in a region of the nanocrystalline Pt sample during annealing (Fig. 1 and movie S1). The HAADF-STEM image of the initial structure (Fig. 1A) shows that three grains—marked G1, G2, and G3—are on [110] zone axis. G2 and G3 have a twin relation; see the fast Fourier transform (FFT) of the image in the inset of Fig. 1A. After annealing at 600°C for 1363.2 s, we observed the shrinkage of G1 from ~9.5 nm to ~6.5 nm (Fig. 1B). The grain orientation (Fig. 1C) shows that G2 does not rotate obviously, whereas the orientation of G1 changes by ~3°. Rotation of G1 is jerky; three major rotation events occur at the moments indicated by the black ("D") and gray ("S6A" and "S6B") dashed lines in Fig. 1C. We sought to determine the structural origin of these three moments. The change in the atomic structure of the Σ11 symmetric tilt grain boundary (STGB) corresponding to the black dashed line labeled by "D" in Fig. 1C is shown in Fig. 1, D1 and D2. The Σ11 STGB migrates by two (113) interplanar spacings during the rotation event with no other detectable changes in GB structure. From the atomic displacement field (Fig. 1D3), we see that along with the GB migration, the atoms on two sides of the GB are displaced in opposite directions. The ratio of the relative tangential displacement to the GB migration distance is ~0.346, consistent with a theoretical shear-coupling factor of 0.354 [supplementary text section 2 (*35*) and figs. S3 to S5] (*9*, *27*). Such consistency suggests that grain rotation results from shear-coupled GB migration. Similarly, we find that the rotation events labeled "S6A" and "S6B" in Fig. 1C coincide with the shear-coupled GB migration events, as shown in fig. S6, A1, A2, B1, and B2. Therefore, the jerky rotation of G1 is correlated with the jerky shear-coupled migration of the Σ11 STGB. Another in situ STEM observation of a more pronounced grain rotation [~8°; details in movie S2, supplementary text section 4 (*35*), and fig. S7] also reveals that each grain rotation event coincides with shear-coupled GB migration.

Our observations suggest that grain rotation arises from shear-coupled GB migration. This is consistent with the theoretical description for a bicrystal with an embedded circular grain (*13*). However, in a polycrystal, each GB is

terminated by TJs. Ideally, when a shear displacement induced by the migration of a GB encounters a TJ, it can be decomposed into two displacements tangential to the other two GBs (following the rule of vector addition). Within a grain, it appears that the displacement direction changes at each TJ and keeps tangential to the surrounding GBs—such a displacement field describes a rotation. As shown in Fig. 1D3, the atoms below the GB are displaced toward the right, and the amount of displacement decays with the distance to the GB. Such a displacement gradient indicates elastic shear strain or rotation. At the left (right) end of the GB, the displacement below the GB has an upward (downward) component; so, the displacement field mainly manifests rotation rather than shear strain. However, in practice, at a TJ, the displacements from the three GBs do not exactly satisfy the vector addition, inevitably generating stress concentration at the TJ. On the other hand, within a grain, the displacements tangential to all the surrounding GBs in general do not lead to the rotation of the same sign. Grain rotation is strongly constrained, requiring coordination of the shears along all GBs (fig. S9 and movie S1).

Atomic scale: Grain rotation and disconnection motion

Because grain rotation is the consequence of shear-coupled GB migration, and the mechanism underlying shear-coupled GB migration is disconnection motion, we expect to see the concurrence of grain rotation and disconnection motion at atomic scale. We show the detailed atomic-scale process of the concurrent grain rotation and GB migration in Fig. 1, D4 to D6. We found that a part of the GB migrates downward, while the other part does not move (Fig. 1D5); the two parts of the GB are separated by a step. The process from Fig. 1,

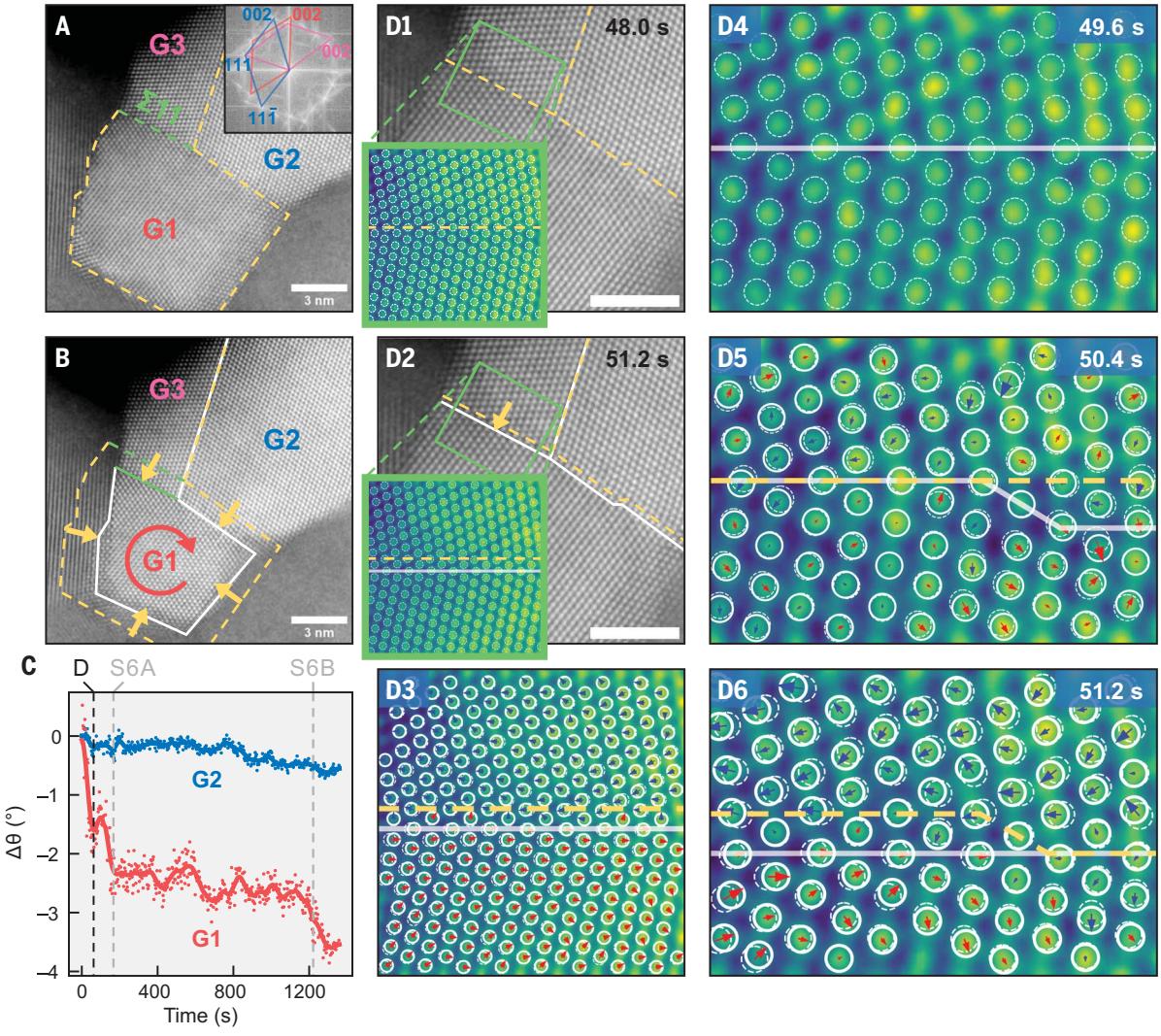

Fig. 1. In situ observation of concurrent GB migration and grain rotation. (**A**) HAADF STEM image of a region of the initial Pt sample containing a Σ11 (113) symmetric tilt GB (green dashed line) and others (yellow dashed lines). Three grains on the [111] zone axis are marked as G1, G2, and G3. The inset shows the FFT pattern of the image, with the diffraction spots of G1, G2, and G3 marked in red, blue, and pink, respectively. (**B**) The final state of the same region, with all GBs marked by solid lines and their initial positions marked by dashed lines. (**C**) Temporal evolution of the orientations of G1 and G2 in (A). Scattered points show the measured data, and the curves are the data processed using a Gaussian low pass filter. Three grain rotation events are marked by black and gray dashed lines, the detailed atomic processes of which are shown in (D) and fig. S6, A and B. (**D1** and **D2**) Sequential images of GB migration during the first grain rotation event marked in (C). The GB locations before and after migration are marked by dashed and solid lines. The insets show the GB structures in the green squares. Scale bars, 3 nm. (**D3**) Atomic displacement fields near the Σ11 GB in the green squares in (D1) and (D2). The atomic positions before and after GB migration are shown by the white dashed and solid circles, respectively. The leftward (rightward) atomic displacements are marked by blue (red) arrows. (**D4** to **D6**) Sequential images of GB migration between (D1) and (D2), with the GB locations and atomic displacements marked.

D5 to D6, shows that the GB migrates by the propagation of the step to the left. However, the step is not necessarily a disconnection. The atomic displacements concentrate in the region where GB migration already occurred, that is, the displacement field propagates together with the step. In other words, the step propagation leads to the translation of the upper grain with respect to the lower grain, suggesting that this step is also of dislocation character. This implies that this step is actually a disconnection. The Burgers vector magnitude of the disconnection is typically much smaller than lattice parameters and cannot be directly measured in the experiment.

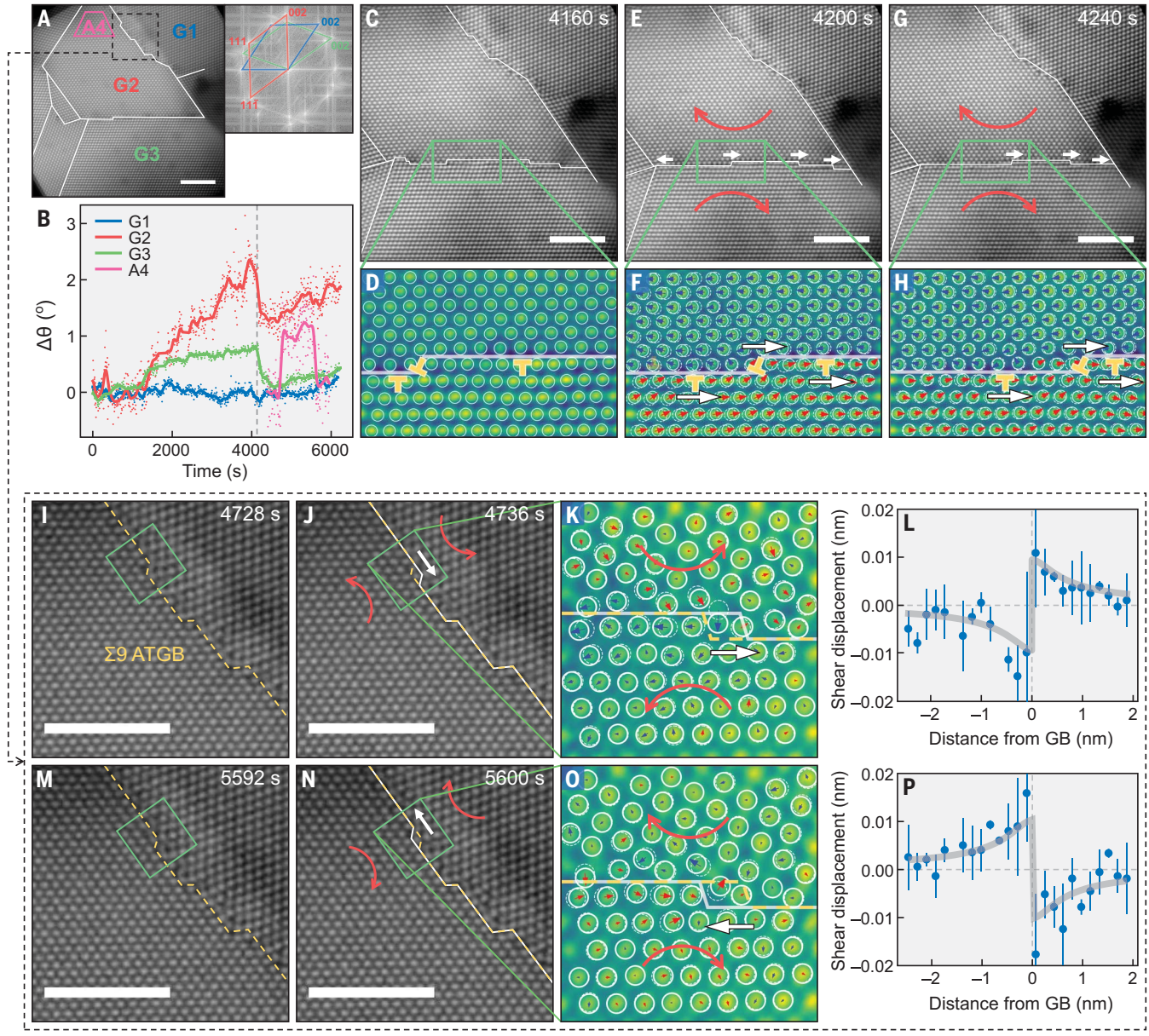

Fig. 2. Atomic-scale observation of concurrent disconnection motion and grain rotation. (**A**) The HAADF STEM image of the final state of the Pt sample, with the GBs marked by white lines. Three grains on the [110] zone axis are marked as G1, G2, and G3. A local area in G2 is marked as A4. The right image shows the FFT pattern of the image, with the diffraction spots of G1, G2, and G3 marked in blue, red, and green, respectively. (**B**) Temporal evolution of the orientations of G1, G2, G3, and A4 in (A). (**C**, **E**, and **G**) Sequential HAADF STEM images of grain rotation at the moment indicated by the gray dashed line in (B). GB locations are marked by white lines. The disconnection motion is indicated by white arrows, and the grain rotation is indicated by red arrows. (**D**, **F**, and **H**) Atomic structures in the green squares in (C), (E), and (G), respectively, showing the disconnection dynamics. Two types of disconnections are marked by the "⊥" symbols. Two sets [(**I** and **J**) and (**M** and **N**)] of sequential images of disconnection motion in the black dashed square in (A), coinciding with two rotation events of A4. The direction of disconnection glide is indicated by white arrows. GB locations before and after the disconnection motions are labeled by yellow dashed and white solid lines, respectively. Grain rotation is indicated by red arrows. (**K** and **O**) Atomic displacements in the green squares in [(I) and (J)] and [(M) and (N)], showing the reversible disconnection motions. Yellow dashed line and white solid line mark the GB locations before and after disconnection motions. (**L** and **P**) The average atomic displacements in the direction parallel to GB, plotted against the distance from GB. Error bars correspond to the standard deviation of the atomic displacements in the same row of atoms. The gray lines show the results of fitting the data to theory. In (A), (C), (E), (G), (I), (J), (M), and (N), the scale bars are 3 nm. In (D), (F), (H), (K), and (O), white dashed circles and solid circles mark the atomic positions before and after disconnection motions, respectively. The leftward (rightward) atomic displacements are marked by blue (red) arrows.

We determine the Burgers vector with the aid of atomistic simulation. From the analysis of bicrystallography (fig. S5) and molecular statics (MS) simulation [supplementary text section 3 (*35*)], we predict the Burgers vector and step height of the disconnection on a Σ11 STGB to be $\mathbf{b} = [\bar{3}3\bar{2}]a_0/22$ and $\mathbf{h} = [1\bar{1}\bar{3}]2a_0/11$, respectively. The shear-coupling factor predicted by $|\mathbf{b}|/|\mathbf{h}|$ is consistent with that measured from the experiment, further verifying the interpretation of disconnection-mediated shear-coupled GB migration.

The conclusions drawn from the Σ11 STGB apply to other types of GBs rarely studied in the literature, such as asymmetric GBs and non-coincidence-site-lattice (non-CSL) GBs. We identified a region of interest consisting of six grains on the [110] zone axis (Fig. 2A). The orientation evolutions of grains G1, G2, G3, and area A4 (Fig. 2B) show that G1 does not rotate and can serve as a reference. Before ~4000 s, G2 and G3 rotate continuously in a counterclockwise manner. The slow rotation is induced by the growth of G2 (movie S3). After ~4000 s, the orientations of G2 and G3 drop abruptly by ~1°. Next, we explore the events on the abrupt change in the orientations of G2 and G3 (near 4000 to 5000 s).

The first GB of interest is the one that separates G2 and G3 (Fig. 2, C to H). This is a (111)/(100) non-CSL GB, as demonstrated by the FFT pattern (Fig. 2A, right image). Per a bicrystallography analysis and MS simulation (fig. S10, B and C), there are two possible types of disconnection on this GB, type I and type II. The type I disconnection has a Burgers vector $\mathbf{b}_\mathrm{I} = [\bar{1}10]a_0/2$ and step height $\mathbf{h}_\mathrm{I} = \mathbf{0}$. Since $\mathbf{b}_\mathrm{I}$ is parallel to the GB plane, the type I disconnection is glissile. Because the step height is zero, propagation of type I disconnections does not contribute to GB migration. The type II disconnection has a Burgers vector $\mathbf{b}_\mathrm{II} = [\bar{1}1\bar{2}]a_0/12$ and a finite step height $\mathbf{h}_\mathrm{II} = [001]a_0/2$. The presence of step character on the non-CSL GB (Fig. 2, C to H) indicates the existence of type II disconnections. We determined the positions of disconnections from the atomic-scale GB structures and labeled them with "⊥" symbols in Fig. 2, D, F, and H. When G2 rotates with respect to G3, all the disconnections glide to the right. The glide of type I disconnections is driven by the internal stress accumulated during the growth of G2 and contributes to the rotation of G2. The glide of type II disconnections is the consequence of the interaction with the type I disconnections. This observation demonstrates that grain rotation is mediated by disconnection motion on the non-CSL GBs.

The second GB of interest is that framed by the black dashed square in Fig. 2A: it is a Σ9 (115)/(111) asymmetric tilt GB (ATGB), as demonstrated by the FFT pattern (Fig. 2A, right image). Area A4 undergoes counterclockwise rotation by ~1° at ~4700 s and clockwise rotation by ~1° at ~5600 s (Fig. 2B). The rotation is highly localized in A4, as the overall orientation of parent grain G2 does not show the same change in Fig. 2B. The change in the ATGB structure corresponding to the counterclockwise rotation of A4 is shown in Fig. 2, I and J, and that with the clockwise rotation is shown in Fig. 2, M and N (Fig. 2, I, J, M, and N are snapshots from movie S3). We see that the reversible rotation of A4 coincides with the reversible glide of disconnections along the ATGB. From the atomic structures in Fig. 2, K and O, we identify the disconnection step height as $\mathbf{h} = [1\bar{1}\bar{1}]a_0/3$ (indexed on the basis of the lower grain). The atomic displacement vectors show the relative displacement between the two grains. This relative displacement occurs through the disconnection glide, and the shear direction depends on the disconnection glide direction. Figure 2, L and P, shows the change in displacement field induced by the rightward or leftward glide of the disconnection. We fitted it to the analytical solution for the glide of an edge dislocation [solid gray curves in Fig. 2, L and P and supplementary text section 5 (*35*)] and found that the horizontal edge component of the disconnection Burgers vector is ~0.51 ± 0.07 Å. Bicrystallography analysis and MS simulations (fig. S11) show that the horizontal component of the Burgers vector of this disconnection should be $\mathbf{b}_\parallel = [\bar{1}\bar{1}2]a_0/18$ (indexed on the basis of the lower grain), and its magnitude is 0.53 Å, close to the value extracted from the experimental data. Since this disconnection has finite step height and Burgers vector, its motion leads to both GB migration and grain rotation.

To achieve atomic-scale resolution, our experimental observations were limited to the GBs of grains with <110> orientations. To verify whether disconnection-mediated grain rotation is limited to the specific type of GBs, we performed MD simulations on the grain growth process in a Pt thin-film sample. We observed disconnection-mediated grain rotation on various types of GBs (fig. S12), suggesting the universality of disconnection-mediated grain rotation regardless of GB type.

Microstructure scale: Grain rotation and grain growth

We had identified the atomic-scale mechanism—disconnection-mediated grain rotation in a nanocrystalline thin film—but it remained unclear whether this mechanism is dominant among all other possible grain rotation mechanisms. For this, we developed an in situ 4D-STEM technique to trace the evolution of multiple grains and collected statistical data for grain rotation on a 400 nm by 400 nm area of the nanocrystalline Pt thin-film sample containing ~2000 grains. We obtained seven 4D-STEM datasets at room temperature, between which the sample was annealed at 600°C for 2.5 min. We derived crystal orientation maps from the 4D-STEM datasets by indexing nanobeam electron diffraction (NBED) patterns [supplementary text section 6 (*35*) and (*36*)]. The orientation mappings at the annealing times of 0, 5, 10, and 15 min (Fig. 3, A to D) show the occurrence of grain growth during annealing. See fig. S13 for the grain orientation and morphology of two representative rotating grains and their corresponding NBED patterns at different annealing times; it shows that both the grain size and grain orientation change during the annealing process and the observed changes in grain size and orientation are correlated.

These results suggest that at the microstructure scale, grain rotation and grain growth are coupled. To verify this point, we performed statistical analysis of grain rotation in 6710 frames of 1950 traceable grains. The distribution of the grain rotation rate (Fig. 3E) shows that 13.6% of the grains exhibit obvious rotation (the rate of change in orientation angle $|\dot{\theta}| > 2°$/min) during grain growth; this demonstrates that grain rotation is ubiquitous and an integral part of the evolution of nanocrystalline structure. We compared the distribution of grain growth rates for all grains $P(|\dot{r}|)$ (Fig. 3F, gray bars) and the distribution for the grains with large rotation rates (>4°/min) $P_\mathrm{rot}(|\dot{r}|)$ (Fig. 3F, red bars). The distribution of grain growth rate (for all grains) is a maximum at $|\dot{r}| \sim 0$ nm/min, while that for rotating grains peaks at $|\dot{r}| \sim 0.35$ nm/min. The ratio of the two distributions $P_\mathrm{rot}(|\dot{r}|)/P(|\dot{r}|)$ (Fig. 3F, blue points) is proportional to the conditional probability $P_\mathrm{rot}(|\dot{r}|)$, that is, the conditional probability of fast rotation ($|\dot{\theta}| >$ 4°/min) when the grain growth rate is $|\dot{r}|$. The conditional probability demonstrates the correlation between grain growth and grain rotation—because $P_\mathrm{rot}(|\dot{r}|)$ monotonically increases with $|\dot{r}|$, fast grain growth or shrinkage admits fast rotation. This result represents the first instance of revealing the correlation between grain growth and grain rotation. Previous literature only reported this correlation for individual grains (*10*, *37*) or failed to reveal the correlation on the basis of independent measurements of grain growth and grain rotation (*38*). On the other hand, the number of rotating grains accounts for only ~20% of the grains with a growth rate of >1 nm/min, which implies that, although grain rotation is coupled to grain growth, grain growth does not necessarily lead to grain rotation. This observation samples all types of GBs, given the random texture and inclination of GB planes of the thin-film sample [figs. S2 and S17; supplementary text sections 1 and 7 (*35*)]. The correlation between grain growth and grain rotation rules out the

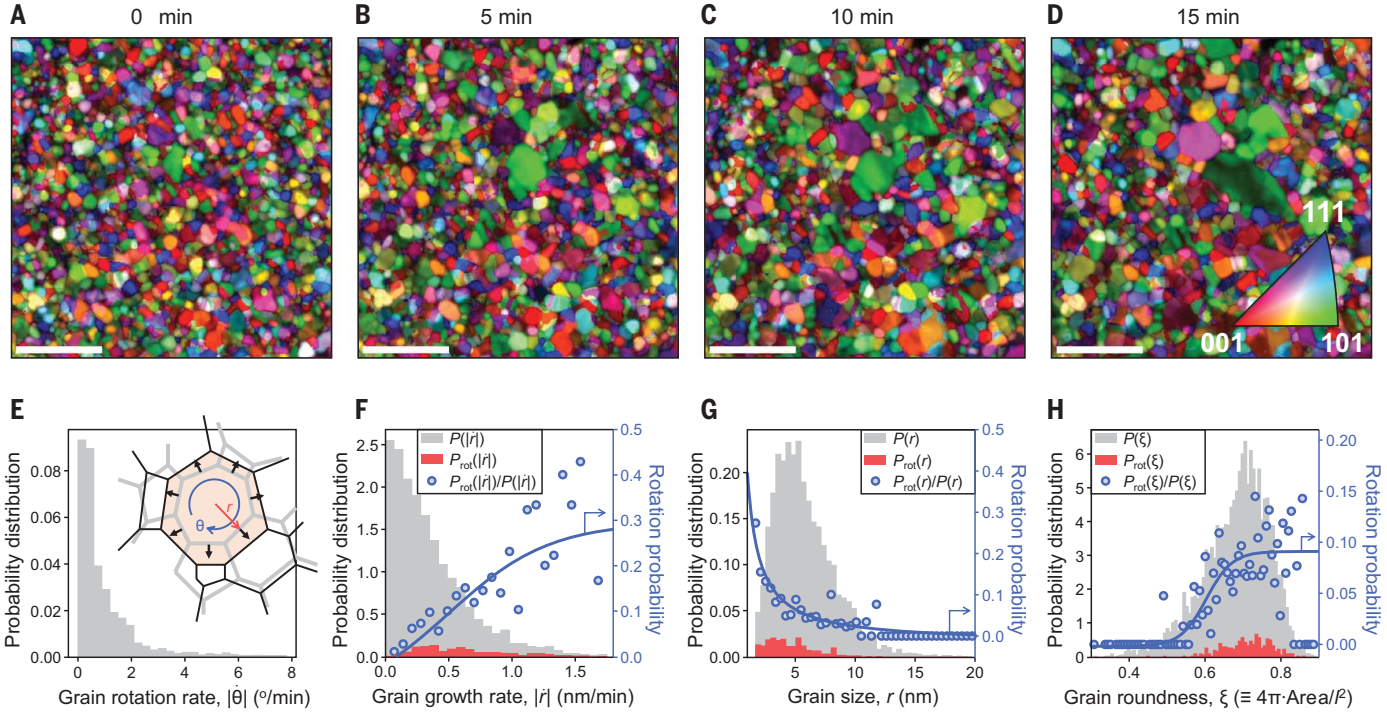

Fig. 3. Microstructure-scale observation of concurrent grain growth and grain rotation. (**A** to **D**) Four sequential 4D STEM orientation mappings of the same area of the Pt sample after annealing for 0, 5, 10, and 15 min, respectively. The color shows the grain orientation on the basis of the inverse pole figure [inset of (D)]. Color saturation is changed according to the indexing confidence. Scale bars, 100 nm. (**E**) The probability distribution for grain rotation rate, $|\dot{\theta}|$. The inset shows the schematic of concurrent rotation and growth of the shaded heptagon grain. (**F**) The probability distributions of grain growth rate ($|\dot{r}|$) for all grains, $P(|\dot{r}|)$, and for the fast rotating grains ($|\dot{\theta}| > 4°$/min), $P_{rot}(|\dot{r}|)$, are indicated by gray and red bars, respectively. The ratio, $P_{rot}(|\dot{r}|)/P(|\dot{r}|)$, plotted as blue points, represents the probability that fast rotation occurs when the grain growth rate is $|\dot{r}|$. (**G**) The probability distributions of grain size for all grains and for the fast rotating grains ($|\dot{\theta}| > 4°$/min) are indicated by gray and red bars, respectively. The ratio, $P_{rot}(r)/P(r)$, is plotted as blue points, representing the probability that fast rotation occurs on the grains with size r. (**H**) The probability distributions of grain roundness for all grains and for the fast rotating grains are indicated by gray and red bars, respectively. The ratio, $P_{rot}(\xi)/P(\xi)$, is plotted as blue points, representing the probability that fast rotation occurs on the grains with roundness ξ. The blue curves are drawn as guides for eyes.

possibility that each grain rotates to reduce the total energy of the surrounding GBs. This correlation is possible only when grain rotation arises from shear coupling to GB migration. This implies that shear-coupled GB migration is the cause of grain rotation. Previous atomic-scale observations show that this correlation arises from the motion of disconnection. It is the step height and Burgers vector features of disconnection that give rise to the simultaneous GB migration and grain rotation. Combining atomic- and microstructure-level observations, we can say that grain growth and rotation are mainly mediated by GBs, which further validates the generality of the disconnection mechanism reported in the section "Atomic scale grain rotation and disconnection motion."

We also studied the dependence of grain rotation probability on grain size and shape. We plotted (Fig. 3G) the distribution of grain size for all grains (gray bars) and for the rotating grains (red bars). The ratio of these two distributions (blue points), $P_{rot}(r)/P(r)$, represents the dependence of grain rotation on grain size. It shows that grain size and grain rotation are negatively correlated. As discussed in supplementary text section 8 (*35*), the negative correlation comes from the inverted factor of r^2 in the dependence of rotation angle and displacement on the circumference (*25*, *39*). We also examined the dependence of grain rotation probability on grain roundness in Fig. 3H. The grain roundness is defined as $\xi \equiv 4\pi A/l^2$, where A is the grain area, and l is the perimeter of a grain. The grain roundness approaches 1 as the shape of a grain becomes more circular and decreases as the shape becomes more irregular. As in Fig. 3, F and G, the ratio of grain roundness (ξ) distribution for rotating grains to that for all grains, $P_{rot}(\xi)/P(\xi)$ (Fig. 3H, blue points), measures the dependence of grain rotation on grain roundness. It shows that round grains tend to rotate. As discussed in supplementary text section 8 (*35*), this arises because a rounder grain can more easily accommodate the shear tangential to the surrounding GBs by grain rotation.

Discussion

We return to the question of which microscopic mechanism underlies near-rigid-body grain rotation in annealing. In our experimental observations, because no slip occurs in the grain interiors and all GBs are high-angle, we can safely ignore all interpretations based on dislocation motion within the crystals. While GB diffusion, shuffling, and sliding were observed and could contribute to grain rotation, these are not quantitative mechanistic descriptions; these may be restated in terms of disconnection motion. A disconnection description is akin to how plastic deformation of crystals is described in terms of dislocation motion rather than simply describing it as atomic rearrangements; of course, any dislocation activity must involve atomic rearrangement (e.g., shuffling or diffusion). We show (Fig. 2, K and O) that disconnection propagation is equivalent to local atomic reorganization (e.g., shuffling or sliding at the GB). On the other hand, GB diffusion can occur through the climb of disconnections with a Burgers vector component perpendicular to the GB (e.g., the type II disconnection on the non-CSL GB shown in Fig. 2). We find that (fig. S15) when a type II disconnection moves left along the non-CSL GB by four atomic columns, an additional atom

column forms, indicating atomic diffusion as required by disconnection climb. A disconnection description of grain rotation and shear coupling provides a level of quantitative predictability not accessible with a shuffling or diffusion description alone. Therefore, it is sufficient to attribute the near-rigid-body grain rotation to disconnection motion—this is consistent with all the findings in our experiments. The critical role of disconnection has been demonstrated in various GB activities including GB migration (*30*), GB-dislocation interaction (*40*), and GB transformation (*41*). Our work further demonstrates the dominance of disconnection activities in near-rigid-body grain rotation, a GB-mediated process, in a nanocrystalline material. Also note that external stress–driven grain rotation has been extensively reported in the literature (*3*, *4*, *12*, *17*, *28*); by contrast, we examined grain rotation in the context of stress-free, capillarity-driven grain growth. While it is expected that stress can drive disconnection motion and grain rotation directly, capillarity can induce grain rotation only when shear-coupling occurs.

Although we conducted our study on a (near-2D) polycrystalline thin film, the conclusions provide important insights for the grain rotation mechanism in bulk polycrystalline materials. Because no observable texture exists in the thin film and the GB plane is randomly inclined (fig. S2), the major difference between the thin-film sample and a bulk sample is that it has free surfaces. As mentioned above, the migration of a GB in a bicrystal is different from that in a polycrystalline film. In a polycrystalline film, the in-plane shear displacement along each GB accompanying GB migration (i.e., shear coupling) is restricted by the TJs. However, the out-of-plane displacement is free. In a bulk polycrystal, the TJs form a 3D network. The shear displacements in all directions are constrained. To extend our conclusions from thin films to bulk samples, we conducted molecular dynamics simulations on both columnar thin-film and bulk samples. As presented in fig. S16 and supplementary text section 9 (*35*), the rotation rate for the thin-film sample is much faster than that for the bulk sample. The likely cause is that rotation of each grain requires coordinated migration of all the surrounding GBs, which is more restrictive for bulk samples where the grains are embedded in all directions. We observe coupling between grain growth and grain rotation for both samples (fig. S16, C and D), consistent with our in situ 4D-STEM results. The similar coupling effect suggests that the dominant mechanism of grain rotation does not change from our observation in thin film to the real bulk sample. In addition, while this study focuses on a single-element system, we expect that the reported grain rotation mechanism is applicable to alloys, offering insights for the design and development of new materials including, for example, compositionally complex materials or high-entropy alloys.

Here, we provide direct multiscale evidence that grain rotation occurs by the propagation of disconnections on GBs in nanocrystalline thin-film materials. Our in situ heating 4D-STEM study demonstrates statistically that grain rotation occurs extensively during grain growth and that this is intimately coupled with GB migration in nanocrystalline materials. The atomic-scale in situ HAADF-STEM observations show that the coupling between grain rotation and GB migration originates from disconnection motion, which leads to shear along GBs and drives grain rotation. These findings demonstrate the critical role of disconnections in determining the properties and behavior of microstructure evolution in nanocrystalline materials and provide new insight for understanding microstructure dynamics and GB engineering.

REFERENCES AND NOTES

1. D. Farkas, S. Mohanty, J. Monk, *Phys. Rev. Lett.* **98**, 165502 (2007).
2. J. C. M. Li, *J. Appl. Phys.* **33**, 2958 2965 (1962).
3. L. Margulies, G. Winther, H. F. Poulsen, *Science* **291**, 2392 2394 (2001).
4. B. Chen *et al*., *Proc. Natl. Acad. Sci. U.S.A.* **111**, 3350 3353 (2014).
5. D. Moldovan, V. Yamakov, D. Wolf, S. R. Phillpot, *Phys. Rev. Lett.* **89**, 206101 (2002).
6. A. Adland, Y. Xu, A. Karma, *Phys. Rev. Lett.* **110**, 265504 (2013).
7. D. Moldovan, D. Wolf, S. R. Phillpot, A. J. Haslam, *Acta Mater.* **50**, 3397 3414 (2002).
8. S. L. Thomas, K. Chen, J. Han, P. K. Purohit, D. J. Srolovitz, *Nat. Commun.* **8**, 1764 (2017).
9. J. Han, S. L. Thomas, D. J. Srolovitz, *Prog. Mater. Sci.* **98**, 386 476 (2018).
10. K. E. Harris, V. V. Singh, A. H. King, *Acta Mater.* **46**, 2623 2633 (1998).
11. M. Upmanyu, D. J. Srolovitz, A. E. Lobkovsky, J. A. Warren, W. C. Carter, *Acta Mater.* **54**, 1707 1719 (2006).
12. L. Wang *et al*., *Nat. Commun.* **5**, 4402 (2014).
13. V. Randle, *Philos. Mag. (Abingdon)* **67**, 1301 1313 (1993).
14. V. Randle, *Mater. Sci. Technol.* **7**, 985 990 (1991).
15. R. C. Pond, D. A. Smith, *Scr. Metall.* **11**, 77 79 (1977).
16. N. Ryum, *Acta Metall.* **17**, 831 837 (1969).
17. T. Gorkaya, K. D. Molodov, D. A. Molodov, G. Gottstein, *Acta Mater.* **59**, 5674 5680 (2011).
18. D. Moldovan, D. Wolf, S. R. Phillpot, *Acta Mater.* **49**, 3521 3532 (2001).
19. C. Herring, *J. Appl. Phys.* **21**, 437 445 (1950).
20. S. Chu *et al*., *Nat. Commun.* **13**, 4151 (2022).
21. M. F. Ashby, R. A. Verrall, *Acta Metall.* **21**, 149 163 (1973).
22. B. N. Kim, K. Hiraga, K. Morita, *Acta Mater.* **53**, 1791 1798 (2005).
23. I. A. Ovid'ko, A. G. Sheinerman, *Scr. Mater.* **59**, 119 122 (2008).
24. M. Murayama, J. M. Howe, H. Hidaka, S. Takaki, *Science* **295**, 2433 2435 (2002).
25. Z. T. Trautt, Y. Mishin, *Acta Mater.* **60**, 2407 2424 (2012).
26. Z. T. Trautt, Y. Mishin, *Acta Mater.* **65**, 19 31 (2014).
27. J. W. Cahn, Y. Mishin, A. Suzuki, *Acta Mater.* **54**, 4953 4975 (2006).
28. Y. Guo *et al*., *Acta Mater.* **241**, 118386 (2022).
29. S. E. Babcock, R. W. Balluffi, *Acta Metall.* **37**, 2367 2376 (1989).
30. Q. Zhu *et al*., *Nat. Commun.* **10**, 156 (2019).
31. F. Mompiou, M. Legros, D. Caillard, *Acta Mater.* **58**, 3676 3689 (2010).
32. C. M. F. Rae, D. A. Smith, *Philos. Mag. (Abingdon)* **41**, 477 492 (1980).
33. M. Guillope, J. P. Poirier, *Acta Metall.* **28**, 163 167 (1980).
34. C. Qiu, M. Salvalaglio, D. J. Srolovitz, J. Han, *Proc. Natl. Acad. Sci. U.S.A.* **121**, e2310302121 (2024).
35. Materials and methods are available as supplementary materials.
36. Y. Bi *et al*., *Microsc. Microanal.* **29** (suppl. 1), 1509 1510 (2023).
37. V. N. Danilenko, D. V. Bachurin, A. A. Nazarov, *Rev. Adv. Mater. Sci.* **55**, 69 77 (2018).
38. T. Shibayanagi, K. Sumimoto, Y. Umakoshi, *Scr. Mater.* **34**, 1491 1495 (1996).
39. J. W. Cahn, J. E. Taylor, *Acta Mater.* **52**, 4887 4898 (2004).
40. Q. Zhu *et al*., *Acta Mater.* **199**, 42 52 (2020).
41. Z. Fang *et al*., *Sci. Adv.* **8**, eabn3785 (2022).
42. Y. Tian *et al*., Grain Rotation Mechanisms in Nanocrystalline Materials: multiscale observations in Pt thin films, version 2, Zenodo (2024); https://doi.org/10.5281/zenodo.13671455.

ACKNOWLEDGMENTS

Funding: This work was supported by the National Science Foundation through the Materials Research Science and Engineering Center program under Grant DMR 2011967 (X.P. and H.H.) and the Army Research Office (ARO) under Grant W911NF 19 1 0263 (X.P., J.H., and D.S.). This study was also supported by the General Research Fund (GRF) grant from the Hong Kong Research Grants Council 17210723 (D.S.) and the Early Career Scheme (ECS) grant from the Hong Kong Research Grants Council CityU21213921 (J.H.). H.H. acknowledges the financial support by the Helmholtz Research Program Materials Systems Engineering and is grateful to the Karlsruhe Nano Micro Facility (KNMFi) for support and access to the facilities. The authors acknowledge the use of facilities and instrumentation at the UC Irvine Materials Research Institute (IMRI) supported in part by the National Science Foundation through the Materials Research Science and Engineering Center program (DMR 2011967). **Author contributions:** Conceptualization: Y.T., J.H., D.J.S., and X.P. Resources: H.H., J.H., D.J.S., and X.P. Data curation: Y.T., X.G., and C.Q. Formal analysis: Y.T., X.G., J.H., and D.J.S. Supervision: J.H., D. J.S., and X.P. Funding acquisition: J.H., D.J.S., and X.P. Investigation: Y.T., X.G., M.X., C.Q., Y.H., Y.B., L.V.E., E.B., and H.H. Methodology: Y.T., X.G., M.X., C.Q., L.V.E., E.B., and H.H. Writing original draft: Y.T. Writing review & editing: J.H., D.J.S., and X.P. **Competing interests:** The authors declare that they have no competing financial interests or personal relationships that would influence the work reported in this paper. **Data and materials availability:** The data behind each figure and the noncommercial codes used for the data analysis are available in Zenodo (*42*). Raw datasets are available from the corresponding authors upon request.

License information: Copyright © 2024 the authors, some rights reserved; exclusive licensee American Association for the Advancement of Science. No claim to original US government works. https://www.science.org/about/science licenses journal article reuse